IOP Publishing Quantum Sci. Technol. 11 (2026) 025012 https://doi.org/10.1088/2058-9565/ae3b6d

Quantum Science and Technology

OPEN ACCESS

RECEIVED
14 July 2025

REVISED
5 December 2025

ACCEPTED FOR PUBLICATION
21 January 2026

PUBLISHED
26 February 2026

PAPER

Graph coloring via quantum optimization on a Rydberg-qudit atom array

Toonyawat Angkhanawin[1,*], **Aydin Deger**[2], **Jonathan D Pritchard**[3] and **C Stuart Adams**[1]

[1] Joint Quantum Centre (Durham-Newcastle), Department of Physics, Durham University, South Road, Durham DH1 3LE, United Kingdom
[2] Department of Physics, Clarendon Laboratory, University of Oxford, Parks Road, Oxford OX1 3PU, United Kingdom
[3] Department of Physics and SUPA, University of Strathclyde, Glasgow G4 0NG, United Kingdom
[*] Author to whom any correspondence should be addressed.

E-mail: physicstj301136@gmail.com

Keywords: quantum annealing, quantum simulation, quantum many-body dynamics, Rydberg atoms, neutral-atom quantum computing, quantum optimization

Abstract

Neutral atom arrays have emerged as a versatile candidate for the embedding of hard classical optimization problems. Prior work has focused on mapping problems onto finding the maximum independent set of weighted or unweighted unit disk graphs. In this paper we introduce a new approach to solving natively-embedded vertex graph coloring problems by performing coherent annealing with Rydberg-qudit atoms, where different same-parity Rydberg levels represent a distinct label or color. We demonstrate the ability to robustly find optimal graph colorings for chromatic numbers up to the number of distinct Rydberg states used, in our case $k = 3$. We analyze the impact of both the long-range potential tails and residual inter-state interactions, proposing encoding strategies that suppress errors in the resulting ground states. We discuss the experimental feasibility of this approach and propose extensions to solve higher chromatic number problems, providing a route towards direct solution of a wide range of real-world integer optimization problems using near-term neutral atom hardware.

1. Introduction

Many real-world problems in industry and finance can be cast as combinatorial optimization problems [1]. Whilst some of these lie in the class of *easy* (P) problems that can be solved efficiently in polynomial time using classical hardware, many exist in the class of *hard* (NP) problems that cannot be solved optimally without an exponential growth of the evaluation time, even when exploiting heuristic algorithms offering polynomial-time approximations. However, such problems could be solved optimally with a polynomial growth of evaluation time in non-deterministic machines [2, 3]. However, despite decades of research in quantum and computer science, it remains an open question whether such non-deterministic machines could be implemented using quantum hardware.

Research into the application of quantum optimization to solving relevant graph problems has explored applications to the maximum independent set (MIS) problem, which consists in finding the largest independent subset of vertices in a graph such that none of the selected vertices are connected by an edge. In the case where each vertex is assigned a weight, this generalizes to the maximum weighted independent set (MWIS) problem. MIS and MWIS are proven to be NP-complete for both planar graphs [4] and unit disk graphs (UDG) [5] with a maximum degree of 3. Recent work has shown that this enables solving underlying MIS and MWIS problems by mapping onto UDG encodings compatible with the native connectivity found in Rydberg atom arrays [6–8] and applying routines such as the variational quantum annealing (VQA) [9–12] or quantum approximate optimization algorithms (QAOAs) [13, 14] to obtain solutions.

Neutral atom arrays have emerged as promising platforms for scalable quantum computing [15–21]. By exploiting the strong, long-range interactions of highly excited Rydberg states it is possible to realize a blockade effect that can be leveraged for high-fidelity digital computing [22–27], programmable quantum simulation [28–34] or analogue optimization, which is the focus of this paper.

UDGs can be natively embedded into neutral atom arrays by geometrically arranging the atoms, with the edges implemented by placing atoms within a blockade radius of each other. This has resulted in a number of experimental demonstrations of solving both MIS [35–38] and MWIS [39, 40] along with exploration of the requirements for achieving a realistic quantum advantage [41–44] from these methods. Beyond this, programmable Rydberg-atom graphs with local addressibility can be geometrically arranged to solve other NP-complete problems such as maximum cut (Max-Cut) [45, 46], integer factorization [47], and, especially, 3-satisfiability (3-SAT) [48] in which the polynomial reduction to the MIS has been proven in [49]. More generally, these approaches reformulate the problem to that of *quadratic unconstrained binary optimization* (QUBO) [50] which can be encoded on atomic arrays using elementary sub-graphs [51] or gadgets [8], with a parity-based approach extending to higher-order constrained binary optimization (HCBO) problems [52].

However, many real-world optimization problems involve integer optimization problems (IP) [53–56] where the decision variables are integers. Given the current development of quantum hardware, there is still no prototype of any physical quantum system into which IPs can be directly encoded. In this work, we focus on solving the *minimum vertex graph coloring problem* (MVGCP) [57], consisting of finding a solution to coloring vertices in a graph such that vertices that share an edge are assigned different colors whilst ensuring the minimum number of colors are used.

Coloring of graphs requiring 3 or more colors is NP-hard, meaning MVGCPs are challenging. These problems arise in a variety of industry applications [1], for instance scheduling optimization [55, 58] or portfolio selection [59]. Directly solving MVGCP on quantum hardware via formulation as a QUBO is resource intensive, with a graph of N vertices and k colors requiring $\mathcal{O}(kN)$ physical qubits [60, 61]. This has driven development of hybrid quantum–classical approaches seeking to solve MVGCP by using heuristic classical solvers combined with quantum hardware to sample the MIS solution requiring only $\mathcal{O}(N)$ physical qubits [60, 62–64]

In this paper, we present a route to natively embed unit-disk graph MVGCP onto a neutral atom platform by performing coherent annealing with Rydberg atom qudits. By coupling to k Rydberg levels, we provide access to a Hilbert space of size $\mathcal{O}(k^N)$ and demonstrate the ability to correctly recover the optimal graph colorings with chromatic numbers $\chi(G) \leqslant k$. This represents a first step towards realizing physical quantum hardware onto which the so-called *quadratic unconstrained integer optimization* (QUIO) can be directly encoded without any mapping to the conventional QUBO [65].

2. Overview of main results

We propose and numerically demonstrate a native embedding of the QUIO formulation of a MVGCP on a k-chromatic graph with N vertices using a qudit-based Rydberg system. This consists of N ground state atoms, each with an EM field coupling to k Rydberg states. The ground and Rydberg states represent our distinct colors. By performing quantum annealing algorithm on the system, we can find optimal graph colorings for planar graphs.

The protocol is illustrated in figure 1. Firstly (a) an original planar graph is mapped to the corresponding unit-disk graph with *compact* structure by the so-called *vertex-to-atom* mapping method, as shown in figure 1(b). Here, compact structure means the arrangement with maximized numbers of equidistant edges. Each pair of neighboring atoms (representing adjacent vertex pairs) is arranged with a spatial separated less than the Rydberg blockade radius, indicated by the green, orange and yellow shades as in figure 1(c). This results in the blockade of a double excitation of the corresponding Rydberg state for any pair of neighboring atoms, i.e. a double excitation of the green Rydberg state is blocked within green shaded region. Similarly, double excitation of the orange (yellow) Rydberg states are blocked within the orange (yellow) shaded region. Simultaneously, we ensure that all the atoms do not fall into the small dark shade of their neighbors, in which the energy spectrum will be affected by undesired negative inter-Rydberg interactions, such that the system's ground state could be altered, making quantum annealing inefficient. The quantum annealing algorithm is performed by driving the quantum dynamics from the initial Hamiltonian with an *easy-to-prepare* ground state, i.e. the product state of the atomic ground state $|gg\ldots\rangle$, to the final Hamiltonian whose ground state encodes the solutions to the given MVGCP. The detunings Δ_i relative to each Rydberg state $|r_i\rangle$ are adiabatically tuned, as shown in figure 1(c), to ensure that the annealing state remains in the instantaneous ground state at all times [10, 11, 66]. Our results show that the annealing process prepares the system in the lowest

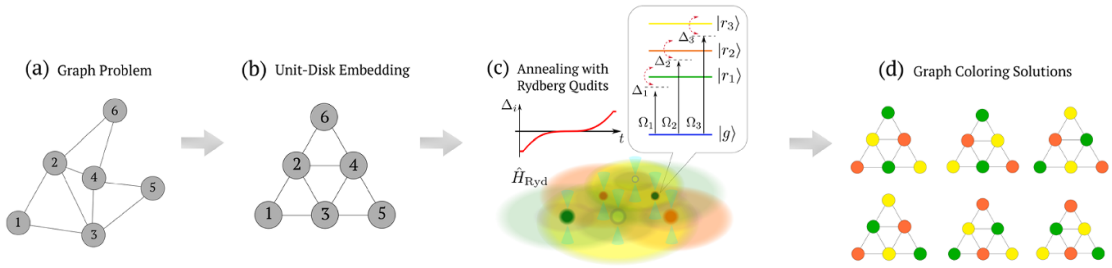

Figure 1. Quantum optimization for graph coloring problems. (a) The original (planar) graph problem is embedded into a corresponding unit-disk graph with compact structure as shown in (b). Here, the vertices and edges of the graph are represented by atoms and their nearest-neighbor interactions. (c) Adiabatic quantum annealing is performed by instantaneously turning on the qudit driving fields Ω_i, and slowly sweeping the detunings $\Delta_i(t)$ from large negative value to positive value (in the direction of red dashed arrows). Here, $i = \{1, 2, .., k\}$ where k is the maximum number of Rydberg states (colors) used. (d) The measurement results at the end of the protocol show a set of degenerate (due to the graph symmetry) optimal solutions to the given MVGCP.

energy state, and that this state encodes the solution to the corresponding MVGCP. In particular, we obtain a degenerate subset of optimal graph coloring solutions, in which their configurations yield exactly the same energy due to the symmetry of the graph, as depicted in figure 1(d). With higher order of the graph symmetry, it has been found that the quantum annealing becomes more efficient such that graph coloring solutions are returned with higher fidelity.

Regarding the feasibility of graph encoding, due to the restricted range of lattice spacings allowed by the encoding constraints in equation (4), solving MVGCPs on equidistant planar graphs is found to be very effective in qudit-based Rydberg systems, as the unwanted negative inter-Rydberg interactions become insignificant compared to the positive conventional (intra) Rydberg interactions. However, to solve MVGCPs on more general planar graphs in which equidistant structures cannot be arranged in two dimensions (2D), we explore alternative encoding strategies such as exploiting three-dimensional (3D) graph embedding to achieve the same connectivity as the original 2D graph whilst maximizing the spacing between qubits that are not linked by an edge. Here, the influence of negative inter-Rydberg interactions on solving MVGCPs have also been analyzed.

The paper is structured as follows. In section 3, the mathematical definition of MVGCPs is introduced along with brief reviews of previous related research on the hybrid quantum–classical and quantum approaches. Next, we address the limitations of current quantum hardware, and how our proposed qudit-based Rydberg system could yield advantages over these limitations. In section 4, we introduce the qudit-based Rydberg Hamiltonian, and show how MVGCPs could be encoded into such a Hamiltonian. Details of the problem encoding onto Rydberg-atom graphs are included here. In section 5, we demonstrate the annealing results of MVGCPs on several equidistant 3-chromatic graphs, composed of a different numbers of (equilateral) triangle subgraphs. Subsequently, in section 6.1, we demonstrate the graph coloring on non-equidistant 4-chromatic graphs to highlight the effect of the negative inter-Rydberg interactions, and show how the graph encoding can be improved by exploiting 3D graph embedding. Finally, in section 7, we summarize the advantages offered by our qudit-based Rydberg systems as an alternative route towards native embedding of integer problems, and also discuss the limitations, experimental feasibility and potential to encode other NP-complete problems on this platform.

3. MVGCP

3.1. Problem statement

Given an undirected graph $G = (V, E)$, where V is a set of vertices and E is a set of edges, a valid solution to the vertex graph coloring problem involves coloring all vertices such that no pair of edge-connected vertices are assigned the same color. A graph coloring that uses k unique colors is called k-coloring with the formal definition

Definition 1. (k-coloring) For an undirected graph $G = (V, E)$, the k-coloring is a mapping $f_k : V(G) \to \mathbb{C}_k$ with $f_k(v) \neq f_k(w)$ for all $(v, w) \in E(G)$. Here, $\mathbb{C}_k = \{1, 2, \ldots, k\}$ is a set of k colors.

In particular, vertex graph coloring is equivalent to partitioning the vertices into k *independent* (stable) sets. The *MVGCP* then consists of finding a valid graph coloring that requires the minimum number of colors. The minimum number k is known as the *chromatic number* $\chi(G)$. Determining the chromatic number of a general graph is widely recognized as NP-hard [67], whilst deciding if a graph is colorable with k-colors is NP-complete for $k \geqslant 3$ [4, 68–70]. MVGCPs on unit-disk graphs mapped from

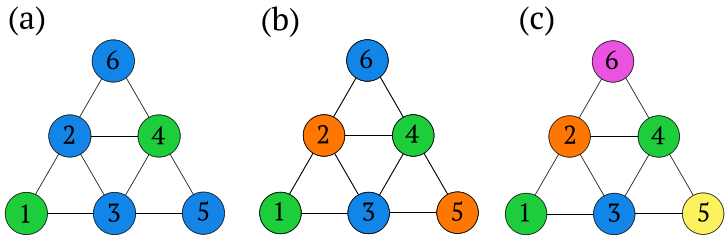

Figure 2. Examples of vertex graph coloring. (a) Invalid graph coloring as adjacent vertices share the same color. (b) An optimal graph coloring with three colors used corresponding to a chromatic number $\chi(G) = 3$. (c) Non-optimal graph coloring where all adjacent vertices are assigned with five different colors. This case is referred to as relaxed graph coloring.

planar graphs with maximum degree at least 3 are proven NP-complete [5, 70]. Figure 2 shows example graph colorings, with an invalid solution where vertices with a connected edge share a color in (a) whilst the optimal solution with $k = \chi(G) = 3$ shown in (b). However, since in general MVGCPs are known to be hard problems, they are, in practice, relaxed to finding k-colorings where $\chi(G) \leqslant k \leqslant |V|$ [71]. This results in sub-optimal graph colorings as shown in (c), and is known as a relaxed coloring which is a valid graph coloring with $k > \chi(G)$.

3.2. Classical approaches

There are a variety of polynomial-time approximate algorithms (PTAAs) which return a non-optimal graph coloring with k no greater than an approximate upper bound relative to the true chromatic number of a problem graph [72, 73]. However, due to the NP-hardness of MVGCPs, exact algorithms [74] turn impractical on graphs with hundreds of vertices, hence many heuristic algorithms have become more common in previous research [75, 76]. Among these approaches, heuristic greedy algorithms are widely used such as the Welsh-Powell [77] or Dsatur algorithms [78] which color vertices sequentially, but with different approaches to choosing the vertex ordering based on their degree or saturation degree, respectively. For each graph there exists a perfect vertex order that would return optimal colorings, and the Dsatur algorithm has been proven exact on certain families of graphs such as chordal graphs, cycle graphs and wheel graphs [79]. Another widely used heuristic method is the recursive largest first (RLF) algorithm [80] which sequentially colors the graph by finding the MIS, assigning these vertices to a given color, and then repeating to find the MIS of the remaining vertices after the previous set is removed.

3.3. Quantum approaches

The simplest approach to solving MVGCP on qubit-based quantum hardware is to cast it as a QUBO of the form [81]

$$H_{\mathrm{QUBO}} = \sum_{v} \left(1 - \sum_{i=1}^{k} x_{v,i}\right)^2 + \sum_{(u,v)\in E(G)} \sum_{i=1}^{k} x_{u,i} x_{v,i}, \tag{1}$$

where $x_{v,i}$ is a Boolean variable representing vertex v with color i. This requires kN physical Ising spins for the problem to be embedded in the Ising model, and typically the quadratic constraint term leads to a requirement for all-to-all connectivity of the qubits encoding the Boolean variables making this highly challenging for near term quantum hardware. Initial benchmarks of this approach for small problems sizes however showed superior performance for quantum annealing on a D-Wave system compared to simulated annealing [62].

To mitigate the physical resource and hardware requirements, Fabrikant *et al* [82] introduced a quantum heuristic method to solve a MVGCP with at most 3 colors, using 2 qubits for encoding each vertex of the graph resulting in an asymptotic performance being polynomial in time. Other work has explored quantum annealing using path-integral Monte Carlo methods [71], however this approach is not effective for graphs with large degeneracies. Instead a constrained quantum annealing method has been developed that uses a driving Hamiltonian that encodes constraints without requiring penalty terms, offering a reduction to N physical qubits [83]. Tabi *et al* [84] implement a space-efficient embedding requiring only $N\log k$ qubits combined with QAOA, however this comes at the cost of deeper circuits which limits performance.

3.4. Hybrid quantum–classical approaches

Within the development of quantum algorithms there exist several hybrid quantum–classical protocols which seek to off-load part of the classically hard computation onto a qubit-based quantum processor, overcoming the intensive physical resource requirements for directly mapping MVGCP on a graph with N vertices using k colors into a QUBO acting on kN Ising spins. Many of these hybrid approaches exploit quantum hardware to iteratively identify the MIS as input for classical heuristic algorithms in a similar approach to RLF. For example, Kwok and Pudenz use MIS solutions to seed a Greedy algorithm [60]. Vitali *et al* used a quantum annealer to iteratively solve for *maximal* independent sets (not necessarily the MIS) which are used as a feasible color assignment in a classical branch and bound (BB) method [85]. Coelho *et al* [64] propose an alternative approach based on the column-generation framework, in which the problem is decomposed into the so-called restricted master problem (RMP) and pricing subproblem (PSP). Here, the RMP is iteratively solved by the classical algorithm with an updated variable (added column) which is a solution to the dual PSP solved with a quantum machine finding the MIS at each step.

3.5. Qudit-based approaches

An alternative approach is to consider algorithms based on using qudits. Wang *et al* [86] introduced a generalization of the Grover algorithm operated on ternary quantum circuits that uses qudits to reduce the complexity of a quantum circuit, resulting in a higher efficiency quantum algorithm. Similar work was carried out by Bravyi *et al* [87], in which the recursive QAOA implemented with hundreds of qutrits has been found to be an efficient algorithm for solving 3-coloring problems in NISQ devices. Recent work from Deller *et al* [88] proposes using QAOA with qudit systems to address the electric vehicle charging optimization problem which is mapped onto the MVGCP. This can be extended to formulate a variety of IPs using QAOA, however native qudit based quantum processors have yet to be realized. Amin *et al* realize adiabatic quantum optimization with qudits, in which logical qudits are implemented using many coupled ancilla qubits [89], but at the cost of requiring a significant physical qubit overhead.

In our work, we propose using multi-level Rydberg atoms as a scalable platform for realizing native qudit encodings. To solve MVGCP on a UDG in this case we cast the problem as a spin-glass Potts model [81, 90–92]. To transform from the QUBO representation above in equation (1), we convert the kN binary variables $x_{v,i}$ to N integer variables $n_i^{(v)}$ which encode the color i on vertex v, giving rise to the following Potts-like problem Hamiltonian

$$H_P \simeq -A \sum_{v\in V(G)} \sum_{i=1}^{k} n_i^{(v)} + B \sum_{(u,v)\in E(G)} \sum_{i=1}^{k} n_i^{(u)} n_i^{(v)}. \tag{2}$$

In the limit $B \gg A$, the second term prevents vertices connected by an edge from having the same color while the first term maximizes the numbers of repeated colors, and the Hamiltonian therefore encodes a solution to the MVGCP as a ground state. As we will show below, this problem can be directly mapped onto N atoms each with k Rydberg levels.

4. Graph coloring with Rydberg-atom qudits

In this section, we provide a detailed description of how the MVGCP problem shown in figure 1 can be solved by mapping onto a qudit-based neutral atom array. Specifically, we consider the case of UDGs, which can be readily realized via the geometric arrangement of atoms using optical tweezers.

4.1. Qudit-based Rydberg Hamiltonian

As illustrated in figure 1(c), we consider the case in which an N-vertex UDG can be realized using an array of N independent atoms each representing a vertex v of the graph, and edges implemented by placing the relevant vertex atoms adjacent to one another—nearest neighbors (NN).

Each atom consists of a ground state $|g\rangle$ which is coherently coupled to k unique *same-parity* Rydberg states $|r_i\rangle$, where $i = \{1, 2, .., k\}$ which encodes our qudit state, as shown in figure 4(a) for $k = 3$. Here, use of same parity Rydberg states eliminates flip-flop interactions caused by resonant dipole-dipole interactions, and ensures all interactions can be treated in the van der Waals (vdW) regime with an energy shift $V(R) \propto C_6/R^6$ where C_6 is the dispersion coefficient and R is the interatomic separation.

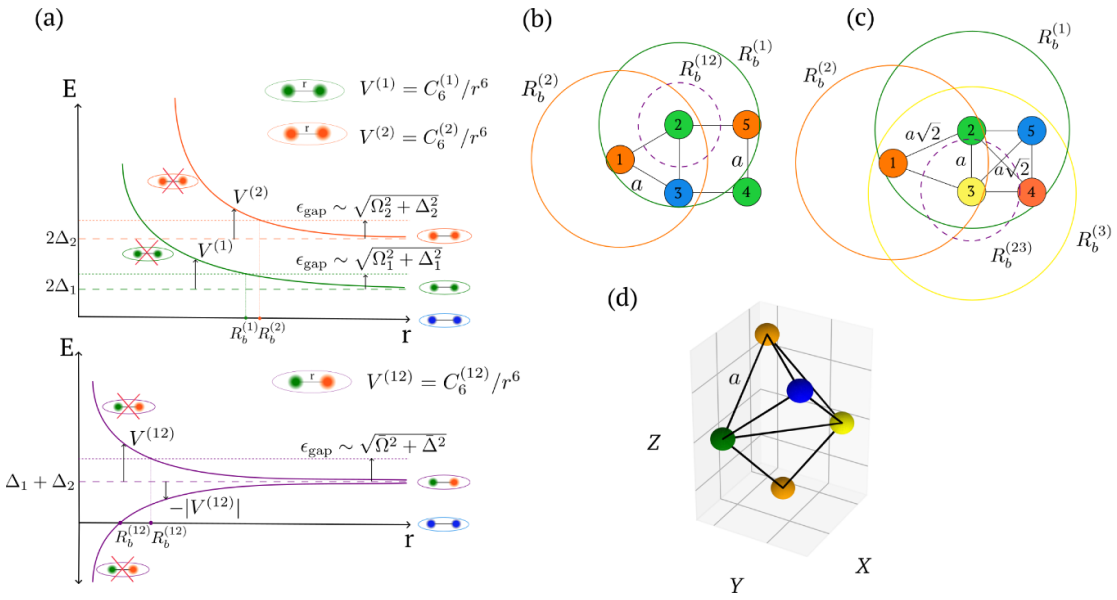

Figure 3. Encoding of Rydberg-atom graph. (a) The energy shifts due to Rydberg interactions between 2 atoms are categorized into two types: 1. (upper) the *intra-Rydberg* interaction denoted by green and orange graphs, respectively, correspond to the double Rydberg excitations $|r_1 r_1\rangle$ and $|r_2 r_2\rangle$. 2. (lower) the *inter-Rydberg* interaction denoted by the purple curve, correspond to the double Rydberg excitation $|r_1 r_2\rangle$. Here, the top (and bottom) graph represents the case of $V^{(12)} > 0$ (and $V^{(12)} < 0$). (b) The equidistant (unit-disk) planar graph implemented by choosing the lattice spacing a such that blockade only connect nearest neighboring (NN) atoms with the conditions: $|V_{\rm NN}^{(ij)}| \ll \Delta_i \ll V_{\rm NN}^{(i)}$, where $i,j = \{1,2\}$. (c) The non-equidistant (unit-disk) graph implemented by shrinking the lattice spacing, a, such that the blockades further connect next-nearest neighboring (NNN) atoms. For NNN atoms, the encoding conditions are: $|V_{\rm NNN}^{(ij)}| \ll \Delta_i \ll V_{\rm NNN}^{(i)}$, and $|V_{\rm NN}^{(ij)}| < \Delta_i$ given the significant increase in $|V_{\rm NN}^{(ij)}|$, see the purple dashed line in the figure. (d) 3D-graph embedding allows the equidistant structure of the non-equidistant graph in (c).

Each Rydberg state is coupled to the ground state using a homogeneous global laser field with Rabi frequency Ω_i and detuning Δ_i from state $|r_i\rangle$, resulting in a Hamiltonian of the form

$$H_{\rm Ryd} = \sum_{v\in V(G)} \sum_i \left(\frac{\Omega_i}{2} \sigma_i^{(v)} - \Delta_i n_i^{(v)} \right) + \sum_{(u,v)\in E(G)} \sum_i V^{(i)}\left(|\boldsymbol{r}_u - \boldsymbol{r}_v|\right) n_i^{(u)} n_i^{(v)} + \sum_{(u,v)\in E(G)} \sum_{i<j} V^{(ij)}\left(|\boldsymbol{r}_u - \boldsymbol{r}_v|\right) \left(n_i^{(u)} n_j^{(v)} + n_j^{(u)} n_i^{(v)} \right) \tag{3}$$

where $\sigma_i^{(v)} = |g\rangle_v\langle r_i| + |r_i\rangle_v\langle g|$, and $n_i^{(v)} = |r_i\rangle_v\langle r_i|$ is the projector onto Rydberg state $|r_i\rangle$ of atom labeling vertex v. The first term in the Hamiltonian describes the coherent atom-light interaction due to the laser fields, where the detuning $-\Delta_i$ corresponds to the energy associated with the atom at vertex i being excited to the state $|r_i\rangle$, and the Rabi frequency Ω_i controls the strength of the driver term coupling $|g\rangle$ to $|r_i\rangle$ which make a key ingredient for quantum steering (annealing) to explore all possible state configurations. The second and third terms, respectively, represent the *intra-Rydberg* interactions between pairs of Rydberg atoms in state $|r_i\rangle$ with coefficients $C_6^{(i)}$, and the *inter-Rydberg* interactions between pairs of atoms in Rydberg states $|r_i\rangle$ and $|r_j\rangle$ with coefficients $C_6^{(ij)}$. They are responsible for penalizing connected vertices that simultaneously excite to the states $|r_i r_i\rangle$ and $|r_i r_j\rangle$, respectively.

The effect of these interaction terms is illustrated in figure 3(a) for the case of two Rydberg levels. In the upper panel we show the pair potential curves for the intra-Rydberg interactions $V^{(1)}(R)$ and $V^{(2)}(R)$ resulting from pairs of atoms in state $|r_1 r_1\rangle$ and $|r_2 r_2\rangle$. When this interaction exceeds the effective Rabi frequency $\sqrt{\Omega_i^2 + \Delta_i^2}$ only a single Rydberg excitation can be created, leading to a blockade for pairs of atoms with a separation below $R_b^{(i)} = (|C_6^{(i)}|/\sqrt{\Omega_i^2 + \Delta_i^2})^{1/6}$. The lower panel shows the inter-Rydberg interaction between atoms in state $|r_1 r_2\rangle$. In this case the corresponding blockade condition is satisfied for $R_b^{(ij)} = (|C_6^{(ij)}|/\sqrt{\bar{\Omega}_{ij}^2 + \bar{\Delta}_{ij}^2})^{1/6}$, where $\bar{\Omega}_{ij} = (\Omega_i + \Omega_j)/2$ and $\bar{\Delta}_{ij} = (\Delta_i + \Delta_j)/2$ are the average Rabi frequency and detuning. Note that during annealing, we define the Rydberg blockade radius within the above formulas at the Landau-Zener transition point where $\Delta_i = 0$.

4.2. Encoding of MVGCP on qudit-based Rydberg system

In the classical limit $\Omega_i \to 0$ the Rydberg Hamiltonian in equation (3) approximates the Potts-like Hamiltonian of equation (2) with $A \to \Delta_i$ and $B \to V^{(i)}(|\boldsymbol{r}_u - \boldsymbol{r}_v|)$ which can be moved inside the summation. Thus, by careful choice of parameters we can engineer the ground-state of the interacting Rydberg system to encode the solution of the classical MVGCP problem in a similar manner to the qubit-based Rydberg system being able to solve MIS [6].

Comparison of the two equations reveals two differences between the classical problem and the Rydberg encoding. The first is the finite-potential tails associated with the vDW interactions, and the second is the additional contribution of the inter-Rydberg couplings. In an ideal system, we would engineer the inter-Rydberg state terms $C_6^{(ij)} = 0$, and embed the UDG using edges of length $a < R_b^{(i)}$ for all i, such that for $0 < \Delta_i \leqslant V^{(i)}(a)$ the ground state matches the MVGCP solution.

However, for real Rydberg states, where in this case we consider the $nS_{1/2}$ Rydberg states of alkali atoms, the inter-Rydberg couplings remain finite and negative with $C_6^{(ij)} < 0$ [93], the corresponding interaction tail can be seen as the bottom graph of the lower panel of figure 3(a). Instead, by choosing states with a large separation in principal quantum number n, we recover $|C_6^{(ij)}| < |C_6^{(i)}|$ for all i,j. This introduces additional restrictions on the choice of parameters, such that now, we require the edge spacing a to be chosen such that $R_b^{(ij)} < a < R_b^{(i)}$, and the detunings to be chosen ideally such that $|V^{(ij)}(a)| \ll \Delta_i \ll V^{(i)}(a)$.

A secondary consequence of the negative inter-Rydberg interactions is that the positive energy penalty of an edge-connected coloring violation between a pair of atoms $|r_i r_i\rangle$ can be cancelled out by the negative energy associated with edge coupling to neighboring atoms in state $|r_j\rangle$. To prevent this blockade violation we introduce a lower bound on the detuning to give the constraint

$$|V^{(ij)}(a)| < \Delta_i < |V^{(i)}(a) + (\alpha - 1)\, V^{(ij)}_{\max}(a)|\ , \tag{4}$$

where α is the maximum degree of the graph and $V^{(ij)}_{\max}(a)$ is the largest inter-Rydberg coupling for each i.

The procedure above requires tuning parameters such that the intra-Rydberg state blockade radii $R_b^{(i)}$ are comparable. To ensure that the pairwise interactions remain additive and ensure suppression of the unwanted $C_6^{(ij)}$ terms, we use $|n_i - n_j| > 2$ [94]. As $C_6 \propto n^{11}$, a simple approach to simply re-scale Rabi frequencies such that $(C_6^{(i)}/\Omega_i)^{1/6} \simeq (C_6^{(j)}/\Omega_j)^{1/6}$ quickly becomes unfeasible. Instead we restrict ourselves to the experimentally realizable Rabi frequencies in the range $\Omega/2\pi = 1 \sim 10$ MHz and adjust the final state detuning terms such that $(C_6^{(i)}/\sqrt{\Delta_i^2 + \Omega_i^2})^{1/6} \simeq (C_6^{(j)}/\sqrt{\Delta_j^2 + \Omega_j^2})^{1/6}$ with $\Delta_i \geqslant \Omega_i$ and $\Delta_j \geqslant \Omega_j$.

For equidistant planar graphs these conditions on spacing and relevant interactions can easily be met when performing direct *vertex-to-atom* mapping, with an example of such an MVGCP embedding for a 5-vertex equidistant graph with maximum degree 3 shown in figure 3(b), where the corresponding blockade radii are indicated as colored circles. Here, the interaction distance is adjusted to give only a NN interaction.

For higher degree UDGs, it is possible to embed graphs with up to degree 8 on neutral atom arrays using a blockade radius adjusted to implement next-NN (NNN) couplings as illustrated in figure 3(c). For an all-to-all square, using non-equal separations, vertex 1 can be connected to just two neighboring atoms, where again the minimum spacing is defined by the largest inter-Rydberg blockade length $R_b^{(ij)}$. In this regime, the strong negative interactions become more significant, and care must be taken to adjust parameters carefully to ensure that the condition of equation (4) are met. Alternatively, 3D embeddings can be used as shown in figure 3(d) which implements the same coupling graph as figure 3(c) but with increased spacing between connected vertices to further suppress the unwanted interactions.

To investigate the use of Rydberg qudits for performing MVGCP optimization we model a $k = 3$ Rydberg annealer as shown in figure 4(a). To meet the requirements above with $|C_6^{(ij}| < |C_6^{(i)}|$ we choose the experimentally accessible $nS_{1/2}$ Rydberg states of Rubidium $|r_1\rangle = |65S_{1/2}, m_j = 1/2\rangle$, $|r_2\rangle = |70S_{1/2}, m_j = 1/2\rangle$ and $|r_3\rangle = |75S_{1/2}, m_j = 1/2\rangle$. For these states we extract C_6 coefficients by fitting the calculated pair-potentials in the range $R = 5 - 8$ μm [95], which for intra-Rydberg interactions gives $\{C_6^{(1)}, C_6^{(2)}, C_6^{(3)}\} = \{360.7, 862.7, 1984.5\}$ 2π GHzμm^6 and for inter-Rydberg interactions $\{C_6^{(12)}, C_6^{(13)}, C_6^{(23)}\} = \{-94.1, -35.0, -226.7\}$ 2π GHzμm^6.

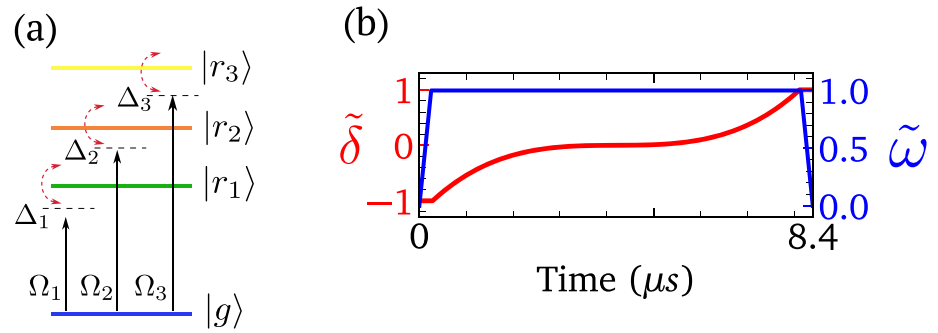

Figure 4. Rydberg-qudit Quantum Annealer. (a) (The 3-Rydberg annealer) Qudit level scheme for $k = 3$ Rydberg states each optically coupled to the groundstate $|g\rangle$ using laser fields with independent detunings Δ_i and Rabi frequencies Ω_i. (b) Quantum annealing profiles showing normalized time-dependence of the detuning $\tilde{\delta}(t)$ and the Rabi frequencies $\tilde{\omega}(t)$ used to prepare the atoms in the MVGCP groundstate.

4.3. Quantum annealing

To prepare atoms in the ground state of the problem Hamiltonian above, we perform quantum annealing [6, 35, 39] whereby the atoms are initially prepared in state $|g\rangle$ and the global laser fields are adiabatically swept from an initial large negative detuning to a final positive detuning. During annealing, non-zero Rabi frequencies Ω_i are required to provide driver terms that enables the system to adiabatically follow the groundstate as the detuning is changed. The parameters are ramped using $\Delta_i(t) = \Delta_i^{\max}\tilde{\delta}(t)$ and $\Omega_i(t) = \Omega_i^{\max}\tilde{\omega}(t)$, where $\Delta_i^{\max}$ and $\Omega_i^{\max}$ are chosen to satisfy the encoding constraints above and the normalized time-dependent functions $\tilde{\delta}$, and $\tilde{\omega}$ are defined as [28, 39]

$$\tilde{\delta}(t) = \begin{cases} -1, & 0 < t < t_i \\ \frac{8}{\tau^3}(t - t_0)^3, & t_i < t < t_f \\ 1, & t_f < t < T \end{cases} \tag{5}$$

$$\tilde{\omega}(t) = \begin{cases} \frac{1}{t_i}t, & 0 < t < t_i \\ 1, & t_i < t < t_f \\ \frac{1}{T - t_f}(T - t), & t_f < t < T \end{cases} \tag{6}$$

where $t_0 = (t_i + t_f)/2$ and $\tau = t_f - t_i$. The annealing profiles are shown schematically in figure 4(c), where we use $t_i = 0.4$ μs, $t_f = 8$ μs, $T = 8.4$ μs. To numerically simulate real-time quantum dynamics, the Trotterization method is used, in which the annealing state is computed by $|\Psi_a(t)\rangle = \prod_{i=0}^{i=p} e^{-iH_{\text{Ryd}}(t_i)\delta t}|\Psi(0)\rangle$. Here, $|\Psi(0)\rangle = |gg\ldots\rangle$, $\delta t = t_i - t_{i-1}$, $t_0 = 0$, and $t_p = T$, where the annealing time is chosen with $T = 8.4\,\mu$s, and the Trotter time steps $p = 300$. Given the error of the method scaling with $\mathcal{O}(T^2/p)$, we Trotterize the time steps by $p = \mathcal{O}(T^2/\epsilon)$ to restrain the error in the admissible scale $\mathcal{O}(\epsilon)$. Analysis of the resulting annealing state $|\Psi_a(t)\rangle$ is performed by calculating the dynamic overlap with the ideal MVGC solutions $|\psi\rangle$ using $P_\psi(t) = |\langle\psi|\Psi_a(t)\rangle|^2$, or by evaluating the probability of observing a specific computational output solution $|i\rangle$ at the final time $t = T$ as $P_i(T) = |\langle i|\Psi_a(T)\rangle|^2$. Calculations are performed using Expokit [96] to enable efficient simulation of the following small-scale examples without the requirement of HPC resources, facilitating proof of concept demonstration of the application of qudit annealing to MVGCP.

5. Equidistant (unit-disk) planar graphs

We first study MVGCPs on planar graphs which can be natively embedded on neutral atom arrays as equidistant unit-disk graphs as shown in figure 5, where all neighboring atoms are spaced with identical distance a. In this section, we will show that to solve MVGCPs on graphs with chromatic number $\chi(G) \leqslant 3$, it is necessary to use $k \geqslant \chi(G)$ Rydberg states. For the 3-Rydberg annealer, we chose Rabi frequencies $\Omega_{1,2,3}^{\max}/2\pi = 1, 2, 5$ MHz giving the corresponding blockade radii $R_b^{(1),(2),(3)} = 8.44, 8.69, 8.55$ μm for intra-Rydberg couplings, and $R_b^{(12),(13),(23)} = 6.30, 4.76, 6.32$ μm for inter-Rydberg interactions. The lattice spacings of embedded unit disks are then tuned such that $R_b^{(23)} < a < 0.8R_b^{(1)}$, leading to the range around 6.32 μm $< a < 6.76$ μm. To satisfy the encoding constraints, we choose

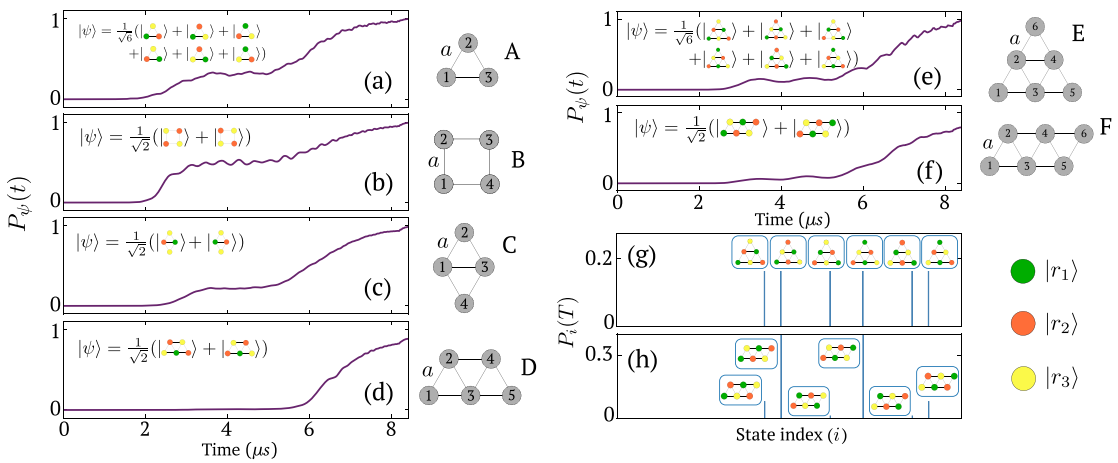

Figure 5. MVGC of equidistant graphs using $k = 3$ Rydberg levels. We consider the following geometries: (a) (equilateral) triangle with three vertices, (b) square, (c) diamond, (d) 3-Fan, (e) triangle-shape triangular lattice and (f) ladder-shape triangular lattice, we show that the 3-Rydberg annealer could solve for optimal colorings with high probabilities approaching 99 %. For the 3-Fan graph (D), another weak population of optimal colorings with the green and orange inverted are also obtained. Here, only the square graph (B) is 2-chromatic while the others are 3-chromatic. Due to different geometric symmetries, the triangle-shape triangular lattice with $\mathbb{S}_3$ symmetry possesses six ($\mathbb{S}_3$) degenerate optimal colorings as depicted in (g), while the ladder shape with lower-order $\mathbb{Z}_2$ symmetry possess three pairs of two ($\mathbb{Z}_2$) degenerate states with unequal probabilities as depicted in (h).

$\Delta^{\max}_{1,2,3}/2\pi = 5, 10, 15$ MHz. Details on these parameter choices can be seen in appendix A, the coordinates for all graphs used in the paper given in table 1 along with the actual lengths of lattice spacing in table 2.

5.1. Cycle graphs (C_N)

Initially we consider cycle graphs where every vertex has degree 2, i.e. triangle (C_3) and square (C_4) geometries. Annealing results are respectively shown in figures 5(a) and (b). For the triangle graph with chromatic number $\chi(G) = 3$, the result is an equal superposition of six possible output states due to the underlying $\mathbb{S}_3$ symmetry, with each color corresponding to a unique Rydberg state. For the square graph with $\chi(G) = 2$, the 3-Rydberg annealer is able to efficiently find optimal solutions with only two Rydberg states, $|r_2\rangle$ (orange) and $|r_3\rangle$ (yellow) due to the larger detunings compared to the Rydberg state $|r_1\rangle$, demonstrating that the k-Rydberg annealer is suitable for efficiently coloring graphs with $\chi(G) < k$.

Extending to higher order C_N cycle graphs, we conclude that the chromatic number $\chi(G) = 2$ with even N, and $\chi(G) = 3$ with odd N, can be solved efficiently with the 3-Rydberg annealer. However, these cycle graphs are not NP-complete as every vertex is degree 2 [5, 69].

5.2. Graphs with maximum degree $\geqslant 3$

To demonstrate the qudit optimization in a non-trivial regime we perform MVGCPs on equidistant planar graphs with maximum degree 3 and 4, i.e. the Diamond (C) and 3-Fan (D) graphs, which are known to be NP-complete [69]. The annealing results are respectively shown in figure 5(c) and (d), where we again demonstrate the ability to find high-fidelity optimal coloring solutions.

From the 3-Fan graph (D), it is possible to extend the geometry by adding an additional vertex to achieve either a triangular (E) or ladder (F) shaped graph as shown in figure 5(e) and (f), both with maximum degree 4. Again we observe in both cases the 3-Rydberg annealer is able to provide optimal coloring solutions, but with sensitivity to the underlying symmetry of the problem.

For the triangle (E), which features $\mathbb{S}_3$ permutation symmetry, the solution results in an equal superposition of six possible valid colorings with 97.2 % fidelity. An interesting observation for this example is that the optimal coloring features only 2 vertices of each Rydberg state, whilst the underlying graph would have a MIS of three vertices. This means that even for this simple geometry, hybrid algorithms that sequentially color graphs using MIS would result in a suboptimal solutions.

For the ladder (F) with $\mathbb{Z}_2$ symmetry (by π-rotation), the solution shows a dominant superposition of only two possible valid colorings. To explore this further, we analyze the relative probabilities of the ground-state solutions in each geometry in figure 5(g) and (h) respectively. Due to the same $\mathbb{S}_3$ symmetry all six solutions appear equally in the triangle configuration (E), but in the ladder configuration (F) not all the six solutions lie in the same $\mathbb{Z}_2$ symmetry and states featuring $|r_3\rangle$ on the

central column of vertices are strongly suppressed. Analysis of the energy spectrum shows that this suppression of the alternative solutions arises due to the different contributions from the next-next-nearest (NNNN) and next-NNNN (NNNNN) neighbor inter-Rydberg interactions, i.e. $V^{(ij)}_{\mathrm{NNNN}} = C^{(ij)}_6/(2a)^6$ and $V^{(ij)}_{\mathrm{NNNNN}} = C^{(ij)}_6/(a\sqrt{7})^6$, which lifts the degeneracy leading to a single pair of solutions encoding the true ground state.

5.3. Graph coloring with $k = \chi - 1$

For all graphs considered in this section with $\chi = 3$, it is instructive to ask if solutions can be found when using $k = 2$ Rydberg states and treat the initial ground-state $|g\rangle$ as a valid color. To explore this question we have performed a comparative analysis in the case of only two Rydberg levels (see appendix B) from which we find that whilst for the cycle graphs A,B and the equidistant graphs C, D, E this provides valid solutions, in the case of the ladder graph F we find invalid colorings featuring edge-connected atoms in $|g\rangle$ meaning the process is not robust in this regime. This failure of the 2-Rydberg annealer to correctly prepare optimal graph colorings arises due to the lack of interaction between neighboring atoms in the ground state $|g\rangle$, meaning the system energetically favors the configurations of the invalid graph coloring states where edge-connected vertices both end up in the ground state.

These results suggest that for robust coloring of any target graph, we require $k \geqslant \chi(G)$ Rydberg states to ensure coloring solutions are represented by populations of strongly interacting Rydberg states.

6. Non-equidistant (unit-disk) graph

In this section, we consider MVGCPs on 4-chromatic planar graphs. In the context of non-planar Rydberg-atom graphs, in which connections to beyond-nearest-neighbor atoms are required, the embedding requires use of non-equidistant geometries such that there is a significant increase in the magnitude of the negative NN inter-Rydberg interaction $V^{(ij)}_{\mathrm{NN}} = C^{(ij)}_6/a^6$ with $C^{(ij)}_6 < 0$, which strongly affects the energy spectrum of the entire system. Since the feasible range of lattice spacing is subject to the encoding constraints, one would expect that it is challenging to extend the effective range of the Rydberg blockade to the NNN atoms without violating the same conditions for the NN atoms, unless one can find a pair of ideal (same-parity) Rydberg states $|r_i\rangle$ and $|r_j\rangle$ with a sufficiently small $C^{(ij)}_6$, ideally zero.

To extend our analysis to consider non-equidistant graphs with $\chi = 4$, for which we use $k = 4$ levels as shown in figure 6(a). For the 4-Rydberg annealer, we choose the following set of Rubidium Rydberg states: $|r_1\rangle = |61S_{1/2}, m_j = 1/2\rangle$, $|r_2\rangle = |66S_{1/2}, m_j = 1/2\rangle$, $|r_3\rangle = |72S_{1/2}, m_j = 1/2\rangle$ and $|r_4\rangle = |78S_{1/2}, m_j = 1/2\rangle$. The C_6 coefficients of these Rydberg states calculated by [95] yield the following intra-Rydberg coefficients $\{C^{(1)}_6, C^{(2)}_6, C^{(3)}_6, C^{(4)}_6\} = \{169.2, 431.4, 1203.7, 3091.1\}$ 2π GHzμm^6, and inter-Rydberg interactions $\{C^{(12)}_6, C^{(13)}_6, C^{(14)}_6, C^{(23)}_6, C^{(24)}_6, C^{(34)}_6\} = \{-35.3, -12.1, -25.3, -76.8, -36.9, -234.1\}$ 2π GHzμm^6. With the chosen Rabi frequencies $\Omega^{\max}_{1,2,3,4}/2\pi = 1, 2, 5, 8$ MHz, the corresponding blockade radii are $R_b^{(1),(2),(3)} = 7.43, 7.74, 7.89, 8.53$ μm for inter-Rydberg interactions and $R_b^{(12),(13),(14),(23),(24),(34)} = 5.35, 3.99, 4.22, 5.29, 4.41, 5.75$ μm for intra-Rydberg interactions.

6.1. Complete graphs with four vertices (K_4)

We explore a range of K_4 graphs embedded in both 2D and 3D as depicted in figure 6(a)–(d), with the coordinates of each graph given in table 1 of appendix A.

The first spatial arrangement depicted as in graph G possesses the $\mathbb{S}_3$ symmetry, hence leading to two sets of 3! (6)-fold degenerate optimal colorings with total fidelity 53.0 % verified by the decomposition of the final annealing state in figure 6(b). As the ratio of the length of the long to short edges is $\sqrt{3}$, there is a strong contribution of negative inter-Rydberg energies such that the annealing populates a number of invalid colorings (red bars) that lie in the spectrum of excited states including the valid colorings (blue bars) featuring $|g\rangle$ on the central vertex.

For the second spatial arrangement as the square shape depicted as in graph H, a higher order $\mathbb{D}_4$ symmetry is observed as the annealing is able to solve for a set of 8-fold degenerate optimal colorings (blue bars) in figure 6(c). In contrast to graph G, graph H with lower ratio of long to short edges equal to $\sqrt{2}$ yields the optimal $\mathbb{D}_4$ colorings with improved fidelity 72.6%. These results suggest that graphs featuring large edge length ratios are more susceptible to errors from the negative inter-Rydberg couplings, and the details of this effect and its impact on the energy ordering of the corresponding graph coloring states is discussed in appendix B.2. Here, we argue that, although finding a proper coloring is NP-hard in general, verification of a proposed coloring is polynomial-time, so obtaining a correct coloring even for a fraction of instances is meaningful because only one correct solution is required [97].

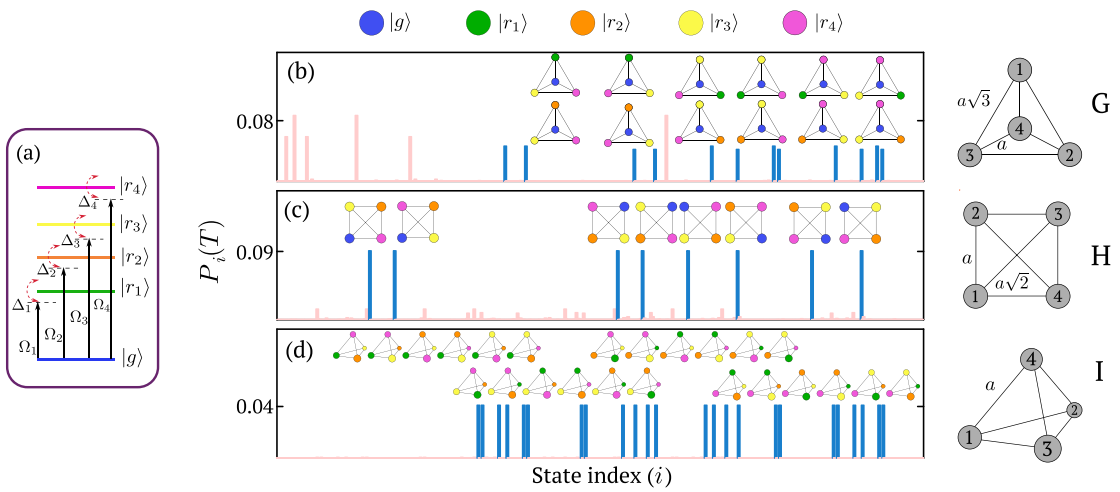

Figure 6. MVGC on non-equidistant complete graphs using $k = 4$ Rydberg levels. (a) The level scheme of the 4-Rydberg annealer using Rabi frequencies $\Omega^{\max}_{1,2,3,4}/2\pi = 1, 2, 5, 8$ MHz and detunings $\Delta^{\max}_{1,2,3,4}/2\pi = 3, 10, 15, 25$ MHz to solve MVGCPs for a set of 4-chromatic complete graphs (K_4) arranged into the following three different spatial geometries: (b) the triangle-shape G, (c) the square-shape H, (d) the 3D tetrahedron I. The 4-Rydberg annealer yields optimal 4-chromatic colorings with 98.2 % probability for the equidistant 3D tetrahedron (I), with 24 degenerate states due to the $\mathbb{S}_4$ permutation symmetry. However, the higher ratio of the length of long edge to short edge, LONG/SHORT, the stronger negative inter-Rydberg interaction that affects the ground state of the system. In the case of the square-shape (H) and the triangle-shape (G) with LONG/SHORT $= \sqrt{2}, \sqrt{3}$, the 4-Rydberg annealer respectively returns $\mathbb{D}_4$ optimal colorings with 72.6 % and $\mathbb{D}_3$ optimal colorings with 53.0 % with strong mixing of incorrect noisy states (red bars). Besides, atoms in ground state $|g\rangle$ (blue color) emerge in the coloring, which is not favorable in term of solving MVGCP.

Building on these results, one can infer that the equidistant structure of embedded graphs is highly desirable. Hence we rearrange the square K_4 graph into 3D space as illustrated in graph I. In this geometry, the graph is not only equidistant but also looks identical at every vertex. In this case, the qudit-based Rydberg Hamiltonian equation (3) is able to approximate the low-energy effective Hamiltonian of the spin-glass Potts model [91] with the highest order of symmetry belonging to the $\mathbb{S}_4$ group, the permutation of a group with four elements, giving rise to the degeneracy of order 24 (4!) in expected solutions. These twenty-four optimal colorings are obtained in the final annealing with the total fidelity up to 98.2% represented by blue bars in figure 6(d).

Together, these results show that it is possible to encode chromatic graphs with $\chi = 4$ and reliably find graph coloring solutions using $k = 4$ Rydberg levels, highlighting the scalability of this approach to higher chromatic numbers as well as the ability to investigate not only planar but also 3D embeddings for efficient graph coloring solutions.

7. Outlook and discussion

In this paper, we have proposed qudit-based Rydberg atom arrays as a route to solve natively embedded MVGCPs. We employ a vertex-to-atom mapping where each color corresponds to a different Rydberg state. In this case, Rydberg quantum wires [6, 98] are not required. In our simulation, we include long-range interaction tails. Qudit positioning is provided by an optical tweezer array. Unit-disk graphs are spatially rearranged into their compact structure where the numbers of equidistant edges are maximized. Our main results are as follows:

Planar graph coloring— We have analyzed the graph coloring on two types of planar graphs, equidistant and non-equidistant, respectively. In sections 5.2 and 6.1, We show that planar graphs $\chi(G) = 3$ and 4 can be robustly solved using the 3- and 4-Rydberg annealer respectively. It is still practical for one to use k-Rydberg annealer to solve MVGCPs for graphs with chromatic number $\chi = k - 1$. Besides, our results show that different orders of graph symmetry correspond to different degeneracies in the graph coloring solutions. Hence as suggested by [99–101], quantum annealing could benefit from symmetry to alleviate the closing of the energy gap between the ground and first excited states as the number of qudits increases. However, due to the limitation of classical computer power, further work is needed to benchmark to larger system size. In section 6.1, the graph colorings on non-equidistant unit-disk graphs, e.g. complete graphs with four vertices (K_4), are performed. Our results show that due to the effect of

the negative inter-Rydberg interactions $V^{(ij)}$, the annealing yields the optimal colorings with lower fidelity compared to the equidistant case. For this reason, we propose a 3D graph embedding method for the K_4 graph where the equidistant structure is recovered using a tetrahedron.

Experimental Approach—The proposed implementation of qudit-based annealing is compatible with current neutral atom experiments. To perform simultaneous excitation of multiple Rydberg states, we consider the case of $k = 3$ low-power seed lasers being locked with independent frequency control relative to a common reference cavity. These can be combined prior to a high-power fiber amplifier stage, enabling common global amplitude control, with Rabi frequencies set by adjusting the relative power of the seed lasers. This can be used in conjunction with beam shaping techniques to enable homogeneous beam delivery across the atom array [31]. For readout of the array, each Rydberg state can be mapped back to independent hyperfine-ground states on timescales fast compared to Rydberg state lifetime using STIRAP [102, 103] combined with fast ground-state rotations [104]. State-selective imaging is then possible using sequential non-destructive imaging of the atom array [105, 106], with states shelved in the lower-hyperfine manifold prior to readout [107].

Potential for coloring non-planar graphs— Our focus has been on planar unit-disk graphs. However, it is possible to extend our technique to solve more general planar graphs. For instance, in the context of solving MVGCPs on non unit-disk planar graphs, one can transform such planar graphs to corresponding unit-disk graphs by utilizing a Rydberg quantum wire. This is implemented by placing a chain of auxiliary atoms to connect vertices separated by more than the blockade length [6, 7, 98]. This approach has also been discussed in [5] in the context of finding unit-disk chromatic number. Here, the results of graph coloring on cycle graphs shown in section 5.1 can be leveraged to implement the Rydberg quantum wire to solve MVGCPs on more complex planar graphs. According to the four-color theorem which states that every planar graph is 4-colorable [108, 109], it suffices for one to use a $(k = 4)$-Rydberg annealer to solve MVGCPs on every planar graph augmented with Rydberg quantum wires. However, the challenge of solving MVGCPs on non-planar graphs with chromatic number greater than 4 remains. Technically speaking, non-planarity spontaneously induces non-equidistant structure, in which the vertex-to-atom mapping will not be the most effective graph embedding, as the quantum annealing would suffer from mapped Rydberg-atom graphs being affected by the negative inter-Rydberg interactions as previously addressed. Hence, augmenting such non-planar graphs with Rydberg quantum wires becomes a more strategic graph embedding method. However, at the crossing of the Rydberg quantum wires one needs to be aware of the intra-Rydberg interaction tails. On the contrary, if one insists on employing vertex-to-atom mapping, a new set of Rydberg states with significantly smaller inter-Rydberg interactions need to be found. Alternatively, one can employ 3D graph embedding, instead of 2D, to enhance the equidistant structure of such non-planar graphs, leading to a better system for encoding non-planar graph coloring problems. In terms of experimental feasibility, solving MVGCPs on k-chromatic graphs with $k > 4$, i.e. general non-planar graphs, becomes extremely demanding. Apart from maintaining coherent control of individual atoms interacting with many lasers or microwave fields, it is also unlikely that we can find a larger set of same-parity Rydberg states compatible with a limited feasible range to satisfy all the encoding conditions previously mentioned in section 4.2. We shall leave this challenge as an open question for future research.

Acknowledgments

We thank Jiannis K Pachos for useful discussions on the many-body simulation aspects of the qudit-based Rydberg Hamiltonian; Antoine Browaeys and Giulia Semeghini for fruitful discussions on the experimental realization of Rydberg-atom quantum simulators; Mark Saffman for discussions on the additivity of Rydberg interactions; and Supanut Thanasilp on suggestions of numerical simulations. TA would like to express deep gratitude to Her Royal Highness Princess Maha Chakri Sirindhorn and the Thai government for providing PhD funding for the first author of this work. JDP and AD acknowledge support from the EPSRC through the following Grants EP/T005386/1, EP/T001062/1 respectively. CSA acknowledge financial support provided by the UKRI, EPSRC Grant Reference No. EP/V030280/1 ('Quantum optics using Rydberg polaritons').

Data availability statement

The data that support the findings of this study are openly available at the following URL/DOI: https://doi.org/10.15129/437db2d0-0b89-4d7e-b505-c9913e8fe212.

Appendix A. Annealing parameters

This section provides additional details motivating choice of annealing parameters as well as the specific geometric arrangements and lattice spacings used throughout the paper.

A.1. Parameter choices

The approach outlined above can be summarized as follows. As outlined above, the first choice when designing parameters for the Rydberg annealer is to identify a subset of k Rydberg levels that satisfy the requirements for $|C_6^{(ij)}| < |C_6^{(i)}|, |C_6^{(j)}|$. Initially states are chosen with $\Delta n = 5$, however for $k = 4$ larger spacings were required to balance the detrimental effects of the strong negative inter-Rydberg C_6^{ij} terms. Next we select Rabi frequencies $0 < \Omega_i/2\pi < 10$ MHz to maintain experimentally realizable power levels such that the corresponding intra-Rydberg blockade lengths $R_b^{(i)}$ are comparable to each other. These blockade lengths are then used to define the lattice spacing a to be used for embedding. For the equidistant graphs we use the range $R_b^{(ij)} < a < 0.8R_b^{(1)}$ to ensure the blockade condition is met for NN atoms with $|V_{\mathrm{NN}}^{(ij)}| \ll \Delta_i \ll V_{\mathrm{NN}}^{(i)}$, whilst experiencing a strong suppression of longer range next-nearest (NNN) and NNNN neighbors $|V_{\mathrm{NNN(NNNN)}}^{(ij)}|, V_{\mathrm{NNN(NNNN)}}^{(i)} \ll \Delta_i$.

As an example we consider annealing the 3-Fan graph (D) using $k = 2$ colors with $n_1, n_2 = 65, 70$. In this geometry the relative interaction strengths are given by $V_{\mathrm{NN}}^{x} = C_6^x/a^6$, $V_{\mathrm{NNN}}^{x} = C_6^x/(\sqrt{3}a)^6 = V_{\mathrm{NN}}^{x}/27$ and $V_{\mathrm{NNNN}}^{x} = C_6^x/(2a)^6 = V_{\mathrm{NN}}^{x}/64$ meaning these terms are strongly suppressed. Rabi frequencies are chosen as $\Omega_{1,2}^{\max}/2\pi = 3, 7$ MHz with $R_b^{(1),(2),(12)} = 7.02, 7.05$ and 5.15 μm. This means we require $5.15 < a < 5.62$ μm, with $11.5 \leqslant V_{\mathrm{NN}}^{(1)}/2\pi \leqslant 19.1$ MHz, $27.5 \leqslant V_{\mathrm{NN}}^{(2)}/2\pi \leq 45.8$ MHz and $-5.0 \leqslant V_{\mathrm{NN}}^{(12)}/2\pi \leq -3.0$ MHz. This introduces bounds on the detunings as $6.7 \leqslant \Delta_1^{\max}/2\pi \leq 11.5$ MHz and $6.7 \leqslant \Delta_2^{\max}/2\pi \leqslant 27.5$ MHz. Above we use $a = 5.26$ μm and $\Delta_{1,2}^{\max}/2\pi = 8, 19$ MHz for implementing graph annealing. Note however that the largest inter-Rydberg coupling in this range $|V_{\mathrm{NN}}^{(12)}|/2\pi = 5.0$ MHz remains close to $\Delta_1^{\max}$, which can cause non-optimal or even invalid solutions to be lower in energy than the true ground state which will be discussed later in appendix B.2.

A.2. Parameter robustness

To investigate the robustness of the annealing protocol to specific drive parameters, we use model a $k = 2$ Rydberg optimization protocol for the Diamond (C) and 3-fan (D) graphs as a function of drive parameters in figure 7. In (a) both states are driven with the same Rabi frequency and detuning with $\Omega_{1,2}^{\max}/2\pi = 3$ MHz, $\Delta_{1,2}^{\max}/2\pi = 10$ MHz, whilst in (b) the Rabi frequency $\Omega_2^{\max}/2\pi = 7$ MHz and finally (c) the optimum parameters $\Omega_{1,2}^{\max}/2\pi = 3, 7$ MHz and $\Delta_{1,2}^{\max}/2\pi = 8, 19$ MHz are used.

In each case as well as the temporal evolution, the final state decomposition is presented with valid solutions colored in blue and invalid colorings in red. Crucially, across this range of parameters the annealing protocol is robust in preparing valid MVGCP solutions with high fidelity, however analysis of the corresponding states shows that for the Diamond graph the use of equal detuning in (a) and (b) leads to weak population of an invalid coloring state featuring two greens at the center of the Diamond due to the negative $C_6^{(12)}$.

For the equal driving case (a) with $\Omega_1 = \Omega_2$ and $\Delta_1 = \Delta_2$, the preference for ground-state is defined by the NNN Rydberg interactions $V_{\mathrm{NNN}}^{(i)} = C_6^{(i)}/(\sqrt{3}a)^6$. Since $C_6^{(1)} < C_6^{(2)}$, this makes the green state a true ground state with an energy gap of $(C_6^{(2)} - C_6^{(1)})/(\sqrt{3}a)^6 = 1.2 \times 2\pi$ MHz from the state with green and orange inverted. By changing to $\Omega_2 > \Omega_1$ in (b), it is possible to preferentially excite the orange state $|r_2\rangle$ earlier due to an effective suppression of the blockade radius with the increased Rabi frequency and a bias towards population of the state as the annealing profile crosses resonance. Finally in (c) with optimized choice of parameters giving $\Omega_2 > \Omega_1$ and $\Delta_2 > \Delta_1$ we recover good energy separation of the instantaneous eigenstates that prevents population of the invalid coloring states.

These results show that using the parameter choices above ensure optimal states are prepared, but the parameters are robust over small changes or fluctuations as required for realistic experimental implementation.

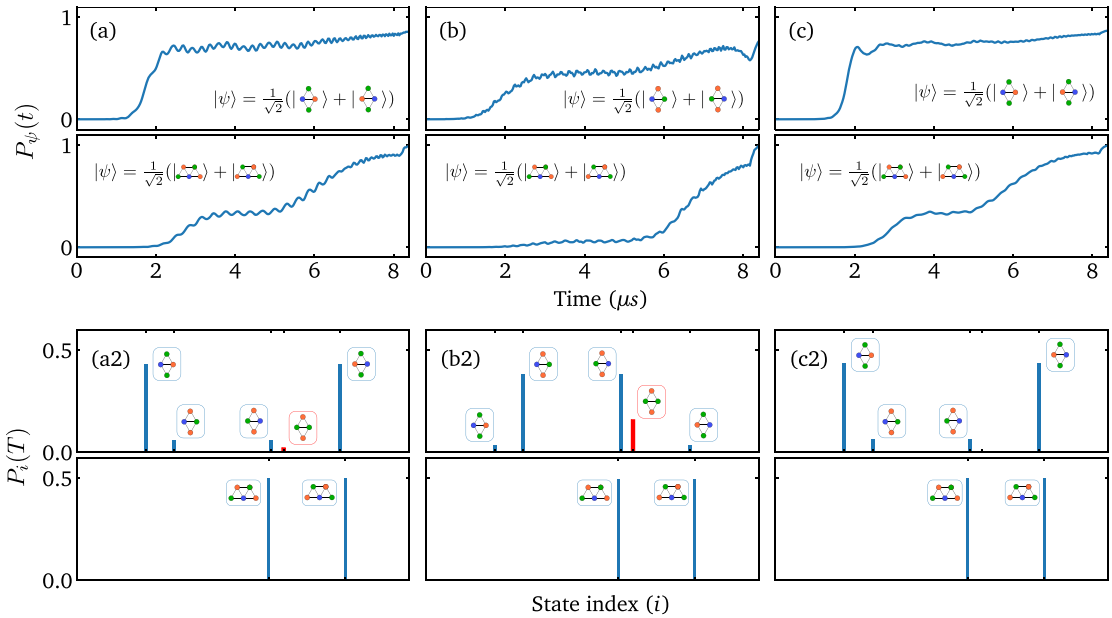

Figure 7. Comparison of different driving parameters. The three different driving protocols follow equations (5) and (6) with (a) $\Delta_1^{\max} = \Delta_2^{\max} = 10 \times 2\pi$ MHz, $\Omega_1^{\max} = \Omega_2^{\max} = 3 \times 2\pi$ MHz, (b) $\Delta_1^{\max} = \Delta_2^{\max} = 10 \times 2\pi$ MHz, $\Omega_1^{\max} = 3 \times 2\pi$ MHZ, $\Omega_2^{\max} = 7 \times 2\pi$ MHz and (c) $\Delta_1^{\max} = 8 \times 2\pi$ MHz, $\Delta_2^{\max} = 19 \times 2\pi$ MHz, $\Omega_1^{\max} = \Omega_2^{\max} = 3 \times 2\pi$ MHz, have been performed to solve MVGCPs of the Diamond graph (C) and the 3-Fan graph (D). Here, the real-time annealing dynamics for the protocols (a) (b) and (c) have been simulated as figure(a), (b) and (c), respectively. The measurement results at the final time $t = T$ for the corresponding protocols follow in figure(a2), (b2) and (c2). Here, a variation in the energy of each Rydberg (color) state affects the ground configurations of solution states as happening in the Diamond graph (C). However, if the reflection symmetry of the graph requires a permutation between two atoms (vertices) excited in the two different energy-varying Rydberg states as happening in the 3-Fan graph (D), the ground configurations are robust to such changes in the driving parameters.

Table 1. The Cartesian coordinates of the vertices of all the problem graphs $G(V, E)$, where $V = \{v_1, v_2, \ldots\}$, considered in the work. Here, the length a of each problem graph is indicated in the corresponding figure in the main text with actual values given in table 2. For the graph J, $\theta = 72^o$ for the pentagon.

Graph	v_1	v_2	v_3	v_4	v_5	v_6
A	$(0,0,0)$	$(a/2, a\sqrt{3}/2, 0)$	$(a,0,0)$	—	—	—
B	$(0,0,0)$	$(0,a,0)$	$(a,a,0)$	$(a,0,0)$	—	—
C	$(0,0,0)$	$(a/2, a\sqrt{3}/2, 0)$	$(a,0,0)$	$(a/2, -a\sqrt{3}/2, 0)$	—	—
D	$(0,0,0)$	$(a/2, a\sqrt{3}/2, 0)$	$(a,0,0)$	$(3a/2, a\sqrt{3}/2, 0)$	$(2a,0,0)$	—
E	$(-a,0,0)$	$(-a/2, a\sqrt{3}/2, 0)$	$(0,0,0)$	$(a/2, a\sqrt{3}/2, 0)$	$(a,0,0)$	$(0, a\sqrt{3}, 0)$
F	$(-a,0,0)$	$(-a/2, a\sqrt{3}/2, 0)$	$(0,0,0)$	$(a/2, a\sqrt{3}/2, 0)$	$(a,0,0)$	$(3a/2, a\sqrt{3}/2, 0)$
G	$(0,a,0)$	$(a\sqrt{3}/2, -a/2, 0)$	$(-a\sqrt{3}/2, -a/2, 0)$	$(0,0,0)$	—	—
H	$(0,0,0)$	$(0,a,0)$	$(a,a,0)$	$(a,0,0)$	—	—
I	$(0,0,0)$	$(-a,0,a)$	$(0,a,a)$	$(-a,a,0)$	—	—
J	$(0,0,0)$	$(a\sin\theta, a\cos\theta, 0)$	$(a\sin 2\theta, a\cos 2\theta, 0)$	$(a\sin 3\theta, a\cos 3\theta, 0)$	$(a\sin 4\theta, a\cos 4\theta, 0)$	$(a\sin 5\theta, a\cos 5\theta, 0)$

Table 2. The actual lengths of lattice spacing a in the unit μm used in all problem graphs for the 2-, 3- and 4-Rydberg annealers.

Graph	A	B	C	D	E	F	G	H	I	J
2-Rydberg annealer	5.26	5.26	4.99	5.26	4.91	5.26	—	—	—	—
3-Rydberg annealer	6.33	6.41	6.75	6.75	6.75	6.75	3.37	4.45	5.61	4.10
4-Rydberg annealer	—	—	—	—	—	—	2.97	3.83	5.90	—

A.3. Graph geometries

Table 1 includes all the Cartesian coordinates of each problem graph considered in this work, and table 2 gives the actual lengths of lattice spacing (in the unit μm) used in the numerical simulations.

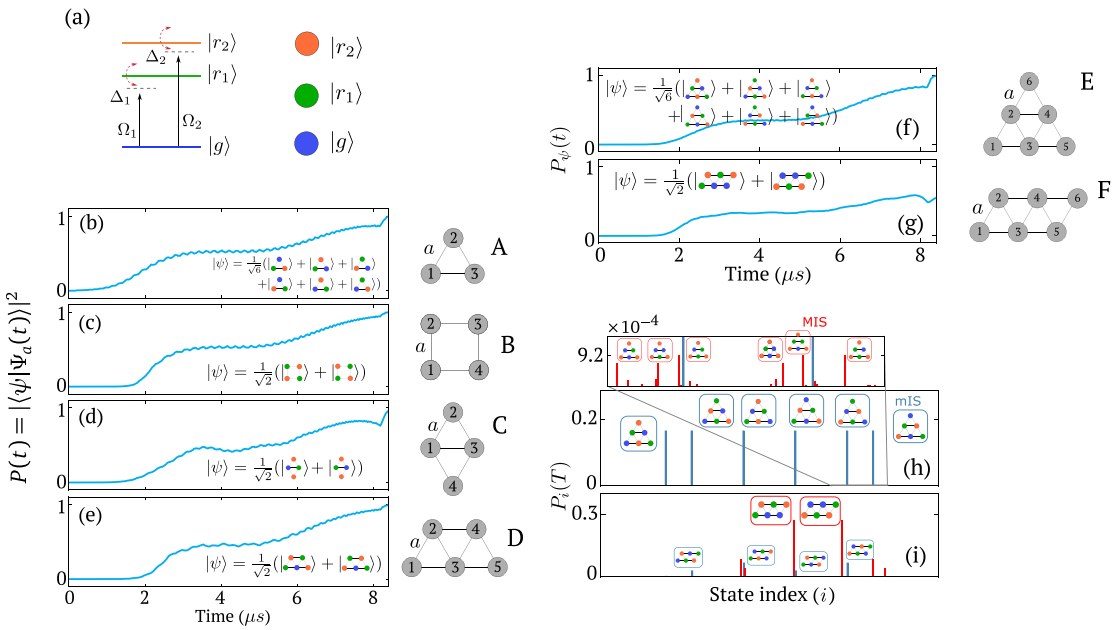

Figure 8. MVGCPs with the 2-Rydberg annealer. (a) The 2-Rydberg annealer with $\Delta_{1,2}^{\max}/2\pi = 8,19$ MHz and $\Omega_{1,2}^{\max}/2\pi = 3,7$ MHz is used to solve MVGCPs for graphs with chromatic number up to 3. i.e. (b) triangle A, (c) square B, (d) diamond C and (e) 3-Fan D. All results give the same solutions as shown in figures 5(a)–(d) with high fidelities near 99 %. In the case of the triangle-shape triangular lattice, the final annealing state yields an equal superposition of six ($\mathbb{S}_3$) degenerate states with fidelity up to 99 % as shown in (f), which is in agreement with the final state decomposition into the computational basis as shown in (h). The zoomed plot of (h) shows that the elements of MIS states (in red circles), with orange vertices belonging to MIS, are suppressed. In contrast to the triangle-shape, the 2-Rydberg annealer fails to correctly color the ladder-shape triangular lattice as the final annealing state yield incorrect colorings containing neighboring ground-state atoms with fidelity up to 55 % as shown in (g), which is in agreement with the final state decomposition of a bar plot in (i).

Appendix B. Solving MVGCPs for k-chromatic graphs using a $(k-1)$-Rydberg annealer

In this appendix we explore MVGCP in the regime where $k = \chi(G) - 1$ Rydberg levels are chosen to investigate whether robust coloring solutions can be obtained if $|g\rangle$ is used as an additional state label. Results are explored for $k = 2$ and $k = 3$ using the same graph structures as above. The results below show that due to the lack of interactions between ground-state atoms, use of $k = \chi(G) - 1$ can perform well for some graphs but has regimes in which invalid ground-state solutions are obtained.

B.1. Annealing on equidistant graphs with $k = 2$

Figure 8 shows the results for graph coloring using the Rydberg annealer with $k = 2$ Rydberg levels (figure 8(a)), where annealing is performed using the Rydberg states $|r_1\rangle = |65S_{1/2}, m_j = 1/2\rangle, |r_2\rangle = |70S_{1/2}, m_j = 1/2\rangle$ with $\Omega_{1,2}^{\max}/2\pi = 3,7$ MHz and $\Delta_{1,2}^{\max}/2\pi = 8,19$ MHz.

For the simple equidistant graphs A-D we find the 2-Rydberg annealer returns solutions with similar fidelity as for $k = 3$, with high fidelities up to 99 % and for graph B where $\chi = 2$ returning only a single set of degenerate solutions due to creation of Rydberg levels being energetically favorable. Extending to consider the 6-vertex graphs in figures 8(e) and (f) we observe that whilst the $k = 2$ solver can provide high quality solutions to the triangle graph E which presents a strong S3 symmetry, the ground-state of the ladder graph F is an invalid coloring solution where we find pairs of edge-connected atoms in $|g\rangle$ along one edge. Analysis of the final state decomposition in the bar plot of figure 8(h) supports this, with the dominant contributions arising from invalid basis states (red bars) with strong suppression of the valid graph coloring states (blue bars). This failure of the 2-Rydberg annealer to correctly prepare optimal graph colorings arises due to the lack of interaction between neighboring atoms in the ground state $|g\rangle$, meaning the system energetically favors the configurations of the invalid graph coloring states (red bars) where any two orange vertices with the strongest repulsive interaction are next-NNN (NNNN) to each other.

These results suggest that it is not conceptually rigorous for one to use $(k-1)$-Rydberg annealer to solve MVGCPs for graphs with chromatic $\chi = k$, despite the fact that the protocol works for small graph instances. However, due to a careful consideration of experimental resources at hand, one is allowed to use the $(k-1)$-Rydberg annealer to predict the lower bound of chromatic number of interested graphs.

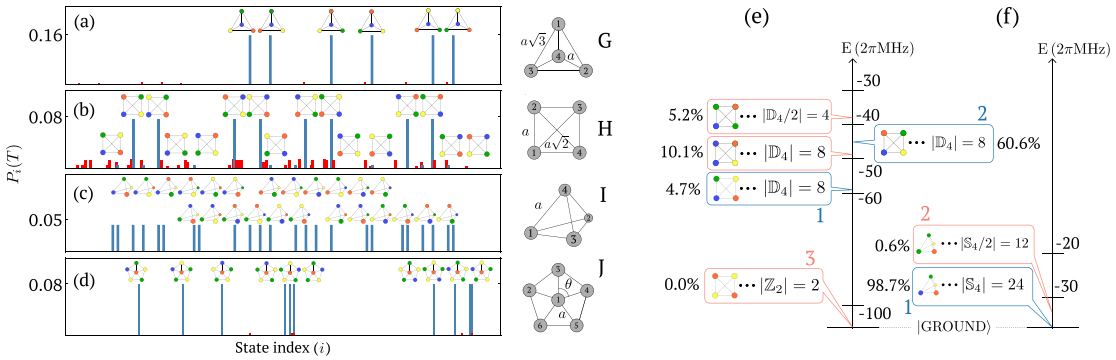

Figure 9. MVGCPs with the 3-Rydberg annealer the MVGCPs for the following 4-chromatic graphs, (a) triangle G, (b) square H, (c) tetrahedron I and (d) pentagon J, is solved with the 3-rydberg annealer. Comparing with results in figure 6, only graph I yields the same correct solutions, while graphs G and H give different results due to the negativity of inter-Rydberg interactions. For the pentagon J with a small ratio of long to short edge lengths equal to $2\sin(36^o) = 1.18$, the annealer is able to solve for two sets of ten degenerate optimal colorings with total fidelity up to 95.1%. Given the influence of the negative inter-Rydberg interactions on the systems' energy spectrum, the optimal colorings for the square K_4 graph (e) are obtained as the excited states denoted by the states 1 and 2 in the blue circles with total fidelity 65.3%, while the true ground state is denoted by the state 3 in the red circle. This negative effect can be suppressed in the 3D graph embedding as illustrated in (f) and (c) where the equidistant structure of the K_4 graph can be rearranged into the tetrahedron. In this case, the twenty-four degenerate optimal colorings are obtained as the system's true ground state with fidelity 98.7%, as indicated by the state 1 in the blue circle.

For instance, if the final annealing state exist a pair of ground-state neighboring atoms after using the $(k-1)$-Rydberg annealer, one could reasonably predict that the graph would have chromatic $\chi \geqslant k$.

B.2. Annealing on non-equidistant graphs with $k = 3$

Moving beyond equidistant graphs we now study annealing of the K_4 graphs presented above with $\chi = 4$ using the $k = 3$ annealer introduced in section 5. Figures 9(a)–(c) shows the resulting decomposition of the final output states, where for graphs G and H we recover valid coloring solutions at the end of the annealing ramp.

Curiously however, whilst the annealing process prepares valid solutions, it turns out for the all-to-all square graph (H) these no longer correspond to the true ground-state. Instead, as shown in figure 9(e), we see that the ground-state solution for this case is actually predicted to be an invalid solution with two atoms each in $|r_2\rangle$ and $|r_3\rangle$ state, In this example the NN distances are chosen as $a = 4.45$ μm, which naturally yield the NNN distances between NNN atoms $\sqrt{2}a = 6.29$ μm. At this spacing, the NNN interactions are: $V_{\text{NNN}}^{(1),(2),(3)}/2\pi = 5.8, 13.8, 31.2$ MHz, and $V_{\text{NNN}}^{(12),(13),(23)}/2\pi = -1.5, -0.6, -3.6$ MHz. With $\Delta_{1,2,3}^{\max}/2\pi = 5, 10, 15$ MHz, the constraint in equation (4) is satisfied for NNN atoms. However, for the NN atoms, there are strong inter-Rydberg interactions $V_{\text{NN}}^{(12),(13),(23)}/2\pi = -12.0, -4.4, -28.5$ MHz which violate the encoding constraints.

In this case the dominant inter-Rydberg state interaction of $V_{\text{NN}}^{(23)}/2\pi = -28.5$ MHz now causes the true ground-state to be the invalid colorings with orange and yellow on the corners, however this negative energy shift is so strong such that it is not possible to populate this state during the annealing ramp as the NN $|r_2 r_3\rangle$ pair state is blockaded with $R_b^{(23)} > a$. Instead we see that the annealing profile preferentially prepares states with $\mathbb{D}_4$ symmetry of order 8, denoted by state 2 in the blue circle in figure 9(e), with fidelity up to 60.6%, whilst the alternative lower-lying valid $\mathbb{D}_4$ state (numbered 1) is also strongly suppressed by the $R_b^{(23)} > a$ blockade.

More generally, for graphs requiring strong NNN interactions, this inter-Rydberg blockade effect means even at $t = 0$ there exist quantum states with lower-energy configurations than the trivial atomic ground state $|gg\ldots\rangle$. For example, at initial time $t = 0$ the actual ground energy of the $\mathbb{Z}_2$ states, denoted by state 3 in the red circle in figure 9(e), amounts to $-2\Delta_2 - 2\Delta_3 + 4V_{\text{NN}}^{(23)} + V_{\text{NNN}}^{(2)} + V_{\text{NNN}}^{(3)} = -19.0$ ($\times 2\pi$ MHz). This leads to two problems: 1.) the adiabatic quantum annealing performed by starting the annealing from this state $|gg\ldots\rangle$ can only adiabatically follow certain instantaneous excited states but not the true ground state of the system, 2.) the true ground state of the system in this case no longer encodes the solutions to the MVGCP on the square K_4 graph, as the solutions are now lying in the excited spectrum of the Rydberg Hamiltonian. Despite the fact that our annealing algorithms have solved for a certain set of optimal graph coloring solutions, the annealing in this case breaks the conceptual definition of adiabatic quantum annealing. To amend this, one either need to find new actual Rydberg states such that the inter-Rydberg interactions $|V^{(ij)}| \ll 1$ (ideally zero) to ensure that the ground states

of the new Rydberg Hamiltonian encodes the solutions to our interested MVGCP, or employ the 3D graph embedding to enhance the equidistant structure out of the K_4 graph, in which the twenty-four $\mathbb{S}_4$ degenerate optimal solutions, as the true ground state of the system, could occupy the annealing state at final time with fidelity 98.7%, as shown in figures 9(c) and (f) without any disruption in the energy spectrum caused by the inter-Rydberg interactions.

Finally, we consider another non-equidistant graph, the so-called *wheel* graph with six vertices (W_6) as depicted in graph J in figure 9(d). Since there exists nearest (NN) and next-nearest (NNN) neighbor edges, the negative inter-Rydberg $V^{(ij)}$ interactions become significant, hence we choose another set of three Rydberg states with reduced inter-Rydberg interactions: $|r_1\rangle = |60S_{1/2}, m_j = 1/2\rangle$, $|r_2\rangle = |65S_{1/2}, m_j = 1/2\rangle$ and $|r_3\rangle = |75S_{1/2}, m_j = 1/2\rangle$, giving the following intra- and inter-Rydberg couplings $\{C_6^{(1)}, C_6^{(2)}, C_6^{(3)}\} = \{138.9, 360.7, 1948.4\}$ GHz μm^6 and for inter-Rydberg interactions $\{C_6^{(12)}, C_6^{(13)}, C_6^{(23)}\} = \{-28.5, -8.0, -34.9\}$ GHz μm^6. With the Rabi frequencies $\Omega_{1,2,3}^{\max}/2\pi = 2, 3, 5$ MHz and the NN (NNN) edge of length 4.10 (4.82) μm, the resulting Rydberg interactions follow $V_{\mathrm{NN}}^{(12),(13),(23)}/2\pi = -6.0, -1.7, -7.3$ MHz, $V_{\mathrm{NNN}}^{(12),(13),(23)}/2\pi = -2.3, -0.6, -2.8$ MHz and $V_{\mathrm{NNN}}^{(1),(2),(3)}/2\pi = 11.0, 28.6, 154.7$ MHz. In order to satisfy the encoding constraints in equation (4) such that NNN atoms, i.e. any pairs of neighboring atoms on the wheel edge, do not stay in the blockade-violated state $|r_1 r_1\rangle$, equation (4) becomes $|V_{\mathrm{NNN}}^{(12),(13)}| < \Delta_1 < |V_{\mathrm{NNN}}^{(1)} + V_{\mathrm{NN}}^{(12)} + V_{\mathrm{NNN}}^{(13)}|$, i.e. $2.3, 0.6 < \Delta_1/2\pi < 4.4$ MHz. Likewise, in order for NNN atoms to not stay in the blockade-violated state $|r_2 r_2\rangle$, the corresponding constraint becomes $2.3, 2.8 < \Delta_2/2\pi < 19.1$ MHz. Since $V_{\mathrm{NN(NNN)}}^{(3)}$ is very strong, the valid range of Δ_3 is relatively flexible. According to this analysis, the detunings that satisfy all the encoding constraints are chosen as $\Delta_{1,2,3}^{\max}/2\pi = 2.5, 10, 15$ MHz. Following the annealing ramp we obtain optimal graph colorings as an equal superposition of 10 degenerate optimal colorings with fidelity 70.4 % as shown in figure 9(d). Besides, there are two additional sets of 10 degenerate optimal solutions with the collection fidelity 16.9 % and 7.8 % whose configurations feature green and yellow atom at the center of the wheel, respectively. Hence, the total fidelity of the optimal graph colorings is up to 95.1%.

ORCID iDs

Toonyawat Angkhanawin 0000-0002-9956-4257
Aydin Deger 0000-0002-6351-4768
Jonathan D Pritchard 0000-0003-2172-7340
C Stuart Adams 0000-0001-5602-2741

References

[1] Wurtz J, Lopes P, Gorgulla C, Gemelke N, Keesling A and Wang S-T2024 arXiv:2205.08500
[2] Garey M R and Johnson D S Freeman W H 1979
[3] Das A and Chakrabarti B K 2008 *Rev. Mod. Phys.* **80** 1061
[4] Garey M R and Johnson D S 1977 *SIAM J. Appl. Math.* **32** 826
[5] Clark B N, Colbourn C J and Johnson D S 1990 *Discrete Math.* **86** 165
[6] Pichler H, Wang S-T, Zhou L, Choi S and Lukin M D 2018 arXiv:1808.10816
[7] Pichler H, Wang S-T, Zhou L, Choi S, and Lukin M D 2018 arXiv:1809.04954
[8] Nguyen M-T, Liu J-G, Wurtz J, Lukin M D, Wang S-T and Pichler H 2023 *PRX Quantum* **4** 010316
[9] Farhi E, Goldstone J, Gutmann S and Sipser M 2000 arXiv:quant-ph/0001106
[10] Farhi E, Goldstone J, Gutmann S, Lapan J, Lundgren A and Preda D 2001 *Science* **292** 472
[11] Albash T and Lidar D A 2018 *Rev. Mod. Phys.* **90** 015002
[12] Larocca M, Thanasilp S, Wang S, Sharma K, Biamonte J, Coles P J, Cincio L, McClean J R, Holmes Z and Cerezo M 2025 *Nat. Rev. Phys.* **7** 174
[13] Farhi E, Goldstone J and Gutmann S 2014 arXiv:1411.4028
[14] Zhou L, Wang S-T, Choi S, Pichler H and Lukin M D 2020 *Phys. Rev. X* **10** 021067
[15] Saffman M, Walker T G and Mølmer K 2010 *Rev. Mod. Phys.* **82** 2313
[16] Saffman M 2016 *J. Phys. B: At. Mol. Opt. Phys.* **49** 202001
[17] Henriet L, Beguin L, Signoles A, Lahaye T, Browaeys A, Reymond G-O and Jurczak C 2020 *Quantum* **4** 327
[18] Morgado M and Whitlock S 2021 *AVS Quantum Sci.* **3** 023501
[19] Dalyac C *et al* 2024 *Eur. Phys. J.* A **60** 177
[20] Kim M, Ahn J, Song Y, Moon J and Jeong H 2023 *J. Korean Phys. Soc.* **82** 827
[21] Adams C S, Pritchard J D and Shaffer J P 2019 *J. Phys. B: At. Mol. Opt. Phys.* **53** 012002
[22] Lukin M D, Fleischhauer M, Cote R, Duan L M, Jaksch D, Cirac J I and Zoller P 2001 *Phys. Rev. Lett.* **87** 037901
[23] Levine H *et al* 2019 *Phys. Rev. Lett.* **123** 037901
[24] Evered S J *et al* 2023 *Nature* **622** 268
[25] Urban E, Johnson T A, Henage T, Isenhower L, Yavuz D D, Walker T G and Saffman M 2009 *Nat. Phys.* **5** 110
[26] Gaëtan A, Miroshnychenko Y, Wilk T, Chotia A, Viteau M, Comparat D, Pillet P, Browaeys A and Grangier P 2009 *Nat. Phys.* **5** 115
[27] Jaksch D *et al* 2000 *Phys. Rev. Lett.* **85** 2208

[28] Bernien H et al 2017 Nature 551 579
[29] Keesling A et al 2019 Nature 568 207
[30] Browaeys A and Lahaye T 2020 Nat. Phys. 16 132
[31] Ebadi S et al 2021 Nature 595 227
[32] Bluvstein D et al 2021 Science 371 1355
[33] Scholl P et al 2021 Nature 595 233
[34] Benhemou A, Angkhanawin T, Adams C S, Browne D E and Pachos J K 2023 Phys. Rev. Res. 5 023076
[35] Ebadi S et al 2022 Science 376 1209
[36] Dalyac C, Henry L-P, Kim M, Ahn J, and Henriet L 2023 arXiv:2306.13373
[37] Byun A, Kim M and Ahn J 2022 PRX Quantum 3 030305
[38] Kim K, Kim M, Park J, Byun A and Ahn J 2024 Sci. Data 11 111
[39] De Oliveira A G, Diamond-Hitchcock E, Walker D M, Wells-Pestell M T, Pelegrí G, Picken C J, Malcolm G P, Daley A J, Bass J and Pritchard J D 2025 PRX Quantum 6 010301
[40] Bombieri L, Zeng Z, Tricarico R, Lin R, Notarnicola S, Cain M, Lukin M D and Pichler H 2024 Quantum adiabatic optimization with rydberg arrays: localization phenomena and encoding strategies (arXiv:2411.04645)
[41] Serret M F, Marchand B and Ayral T 2020 Phys. Rev. A 102 52617
[42] Cain M, Chattopadhyay S, Liu J-G, Samajdar R, Pichler H, and Lukin M D 2023 arXiv:2306.13123
[43] Andrist R S et al 2023 Phys. Rev. Res. 5 043277
[44] Schuetz M J A, Andrist R S, Salton G, Yalovetzky R, Raymond R, Sun Y, Acharya A, Chakrabarti S, Pistoia M, and Katzgraber H G 2025 Quantum compilation toolkit for rydberg atom arrays with implications for problem hardness and quantum speedups (arXiv:2412.14976)
[45] Graham T M et al 2022 Nature 604 457
[46] Goswami K, Mukherjee R, Ott H and Schmelcher P 2024a Phys. Rev. Res. 6 023031
[47] Park J, Jeong S, Kim M, Kim K, Byun A, Vignoli L, Henry L-P, Henriet L and Ahn J 2023 Phys. Rev. Res. 6 023241
[48] Jeong S, Kim M, Hhan M, Park J and Ahn J 2023 Phys. Rev. Res. 5 43037
[49] Choi V 2010 arXiv:1004.2226
[50] Tan B, Lemonde M-A, Thanasilp S, Tangpanitanon J and Angelakis D G 2021 Quantum 5 454
[51] Byun A, Jung J, Kim K, Kim M, Jeong S, Jeong H and Ahn J 2024 Adv. Quantum Technol. 7 2300398
[52] Lanthaler M, Dlaska C, Ender K and Lechner W 2023 Phys. Rev. Lett. 130 220601
[53] Chansombat S, Pongcharoen P and Hicks C 2018 Int. J. Prod. Res. 57 1
[54] Sawik T 2005 Math. Comput. Modelling 41 99
[55] Sawik T 2011 Scheduling in Supply Chains Using Mixed Integer Programming (Wiley) (https://doi.org/10.1002/9781118029114)
[56] Zeng L, Zhang J and Sarovar M 2016 J. Phys. A: Math. Theor. 49 165305
[57] Formanowicz P and Tanaś K 2012 Found. Comput. Decis. Sci. 37 223
[58] Ishihara T and Limmer S 2020 Lecture Notes in Computer Science (Including Subseries Lecture Notes in Artificial Intelligence and Lecture Notes in Bioinformatics) vol 12104 LNCS (Springer) p 37
[59] Cornuéjols G, Peña J and Tütüncü R Optimization Methods in Finance 2018 vol 1, 2nd edn (Cambridge University)
[60] Kwok J and Pudenz K 2020 arXiv:2012.04470
[61] Goswami K, Schmelcher P and Mukherjee R 2024b Quantum Sci. Technol. 9 045016
[62] Silva C, Aguiar A, Lima P M V and Dutra I 2020 Quantum Mach. Intell. 2 1
[63] Vercellino C, Vitali G, Viviani P, Giusto E, Scionti A, Scarabosio A, Terzo O and Montrucchio B 2023 IEEE Comp. Soc. 141–147
[64] Coelho W D S, Henriet L and Henry L-P 2023 Phys. Rev. A 107 032426
[65] Karimi S and Ronagh P 2017 Quantum Inf. Process. 18 94
[66] Hauke P, Katzgraber H G, Lechner W, Nishimori H and Oliver W D 2020 Rep. Prog. Phys. 83 054401
[67] Garey M R and Johnson D S 1976 J. ACM 23 43
[68] Karp R M 1972 Comput. Complex. 85 85–103
[69] Garey M R, Johnson D S and Stockmeyer L 1976 Theor. Comput. Sci. 1 237
[70] Gräf A, Stumpf M and Weißenfels G 1998 Algorithmica 20 277
[71] Titiloye O and Crispin A 2011 Discrete Opt. 8 376
[72] Paschos V T 2003 Computing vol 70 (Springer) p 41
[73] Husfeldt T 2015 Graph colouring algorithms arXiv:1505.05825
[74] Sager T J and Lin S-J 1991 INFORMS J. Comput. 3 226
[75] Galinier P and Hertz A 2006 Comput. Oper. Res. 33 2547
[76] Johnson D, Aragon C, McGeoch L and Schevon C 1991 Oper. Res. 39 378
[77] Welsh D J A 1967 Comput. J. 10 85–86
[78] Brélaz D 1979 Commun. ACM 22 251
[79] Yekezare N, Zohrehbandian M, Maghasedi M and Bonomo-Braberman F 2024 Oper. Res. Lett. 57 107185
[80] Leighton F T 1979 J. Res. Natl Bur. Stand. 84 489
[81] Lucas A 2014 Front. Phys. 2 1
[82] Fabrikant A and Hogg T 2002 Proc. National Conf. on Artificial Intelligence pp 22–27
[83] Kudo K 2018 Phys. Rev. A 98 22301
[84] Tabi Z, El-Safty K H, Kallus Z, Haga P, Kozsik T, Glos A and Zimboras Z 2020 Proc. - IEEE Int. Conf. on Quantum Computing and Engineering, QCE 2020 vol 56
[85] Morrison D R, Jacobson S H, Sauppe J J and Sewell E C 2016 Discr. Opt. 19 79
[86] Wang Y and Perkowski M 2011 IEEE Int. Symp. on Multiple-Valued Logic vol 294
[87] Bravyi S, Kliesch A, Koenig R and Tang E 2022 Quantum 6 678
[88] Deller Y, Schmitt S, Lewenstein M, Lenk S, Federer M, Jendrzejewski F, Hauke P and Kasper V 2023 Phys. Rev. A 107 062410
[89] Amin M H S, Dickson N G and Smith P 2013 Quantum Inf. Process. 12 1819
[90] Inaba K et al 2022 Commun. Phys. 5 137
[91] Wu F Y 1982 Rev. Mod. Phys. 54 235
[92] Mulet R, Pagnani A, Weigt M and Zecchina R 2002 Phys. Rev. Lett. 89 268701
[93] Wadenpfuhl K and Adams C S 2024 Unravelling the structures in the van der waals interactions of alkali rydberg atoms (arXiv:2412.14861)

[94] Cano D and Fortágh J 2012 *Phys. Rev. A* **86** 043422
[95] Šibalić N, Pritchard J D, Adams C S and Weatherill K J 2017 *Comput. Phys. Commun.* **220** 319
[96] Sidje R B 1998 *ACM Trans. Math. Softw.* **24** 130
[97] Ghosal S and Ghosh S C 2024 *Discrete Appl. Math.* **354** 108
[98] Kim M, Kim K, Hwang J, Moon E-G and Ahn J 2022 *Nat. Phys.* **18** 755
[99] Bernaschi M, González-Adalid Pemartín I, Martín-Mayor V and Parisi G 2024 *Nature* **631** 749
[100] Laumann C R, Moessner R, Scardicchio A and Sondhi S L 2012 *Phys. Rev. Lett.* **109** 030502
[101] Janke W and Villanova R 1997 *Nucl. Phys. B* **489** 679
[102] de Léséleuc S, Lienhard V, Scholl P, Barredo D, Weber S, Lang N, Buchler H, Lahaye T and Browaeys A 2019 *Science* **365** 775
[103] Chen T, Huang C, Velkovsky I, Hazzard K R A, Covey J P and Gadway B 2024 *Nat. Commun.* **15** 2675
[104] Levine H, Bluvstein D, Keesling A, Wang T T, Ebadi S, Semeghini G, Omran A, Greiner M, Vuletić V and Lukin M D 2022 *Phys. Rev. A* **105** 032618
[105] Kwon M, Ebert M F, Walker T G and Saffman M 2017 *Phys. Rev. Lett.* **119** 180504
[106] Nikolov B, Diamond-Hitchcock E, Bass J, Spong N L R and Pritchard J D 2023 *Phys. Rev. Lett.* **131** 030602
[107] Graham T M, Phuttitarn L, Chinnarasu R, Song Y, Poole C, Jooya K, Scott J, Scott A, Eichler P and Saffman M 2023 *Phys. Rev. X* **13** 041051
[108] Appel K, Haken W and Koch J 1977 *Illinois J. Math.* **21** 491
[109] Appel K and Haken W 1977 *Illinois J. Math.* **21** 429